TABLE OF CONTENTS

TABLE OF CONTENTS – CONTINUED

# LIST OF TABLES

# LIST OF FIGURES

Figure Page

LIST OF FIGURES – CONTINUED

Figure Page

# Part I

# *MOSES-II* Optical Integration and Testing

# CHAPTER 1
# INTRODUCTION

## 1.1 Optical Design

The *MOSES-II* spectrograph employs an off axis spherical grating (primary mirror) to form solar images in the $m = -1$, $m = 0$, and $m = +1$ spectral orders. These images are recorded on charge coupled devices (CCD) located at prime focus in each order. The optical path is split approximately in half by a flat secondary mirror. The off axis configuration is used so the secondary does not obscure the primary mirror. The *MOSES* instrument design is shown semi-schematically in figure 1.1.

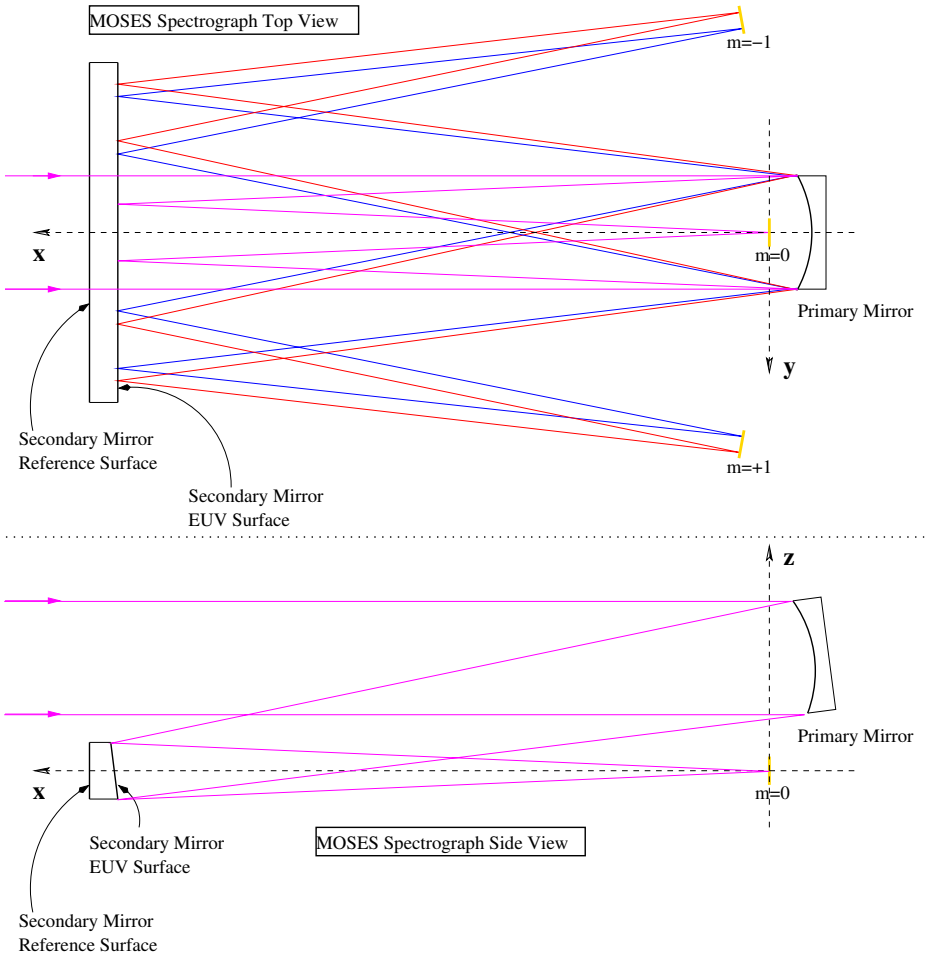


Figure 1.1: Schematic of the *MOSES* spectrograph and coordinate system.

*MOSES-II* optical prescription is shown in table 1.1.

| Item | X | Y | Z | Pitch | Yaw |
|---|---|---|---|---|---|
| Grating | 118.7 | 0.0 | 78.5 | -0.993 | 0.0 |
| Secondary | 2382.5 | 0.0 | 0.0 | +0.993 | 0.0 |
| Det(+1) | 3.0 | -136.7 | 0.0 | -.011 | -2.463 |
| Det( 0) | 0.0 | 0.0 | 0.0 | -.004 | 0.000 |
| Det(-1) | 3.0 | +136.7 | 0.0 | -.011 | +2.463 |

Table 1.1

*MOSES-II* primary mirror is a concave sphere with specified radius of curvature of 9295mm and is ruled (621 l/mm) only within a 60mm diameter circular area centered on the primary clear aperture. The profiles are optimized with intent to distribute incident light in *MOSES-II* passband equally to the $m = -1$ and $m = +1$ orders and nowhere else. The primary mirror clear aperture is an 80mm square, and balance of the aperture is not ruled, and thus puts light only in the $m = 0$ spectral order. The result is an approximately 25%, 50%, 25% distribution of intensity between the $m = -1$, $m = 0$, $m = +1$ orders respectively.

*MOSES-II* secondary mirror is a monolithic flat mirror with clear aperture 189.8 mm $\times$ 48.8 mm, wide enough in the dispersion direction to fold the optical path in all three spectral orders. The mirror substrate is wedge shaped when viewed from the side as in the lower panel of figure 1.1. The angled (right) facet is the multilayer coated surface. The vertical (left) hand facet of the wedge is coated for visible light reflection and is used as an alignment reference surface; therefore the wedge angle between the two surfaces must be accurately known. The specified wedge angle is 0.973 degrees.

The primary mirror surface and the EUV surface of the secondary mirror are coated with Si/Cr/Sc/Cr multilayers for 50 Åfwhm reflectance centered at 470 Å, peaking at about 0.3 [WINDT MULTILAYER: [Moses_local] Fwd: Si/Sc coating results].

### 1.1.1 Changes from *MOSES-I*

It was originally intended that changing *MOSES* observation wavelength would amount to changing coatings; the optical design would remain the same. Due to manufacturing limitations, however, the primary mirror design was changed significantly from the prior flight. The focal length was reduced by almost 100mm and the secondary mirror was moved closer to the primary to accommodate. A new secondary mirror mount had to be designed and fabricated for this purpose.

The specified grating pitch was not updated to reflect the change in focal length. The CCD positions in the $y$ direction are effectively fixed. Moving the secondary towards the focal plane while keeping the diffraction angle fixed introduces an alignment offset of approximately 2.5mm, or about 10% of CCD width, between the dispersed orders and $m = 0$. This misalignment is corrected in software at a reasonable cost in reduced field of view.

Reducing the focal length calls for a change in pitch angle on the primary, or secondary, or both to maintain alignment. I chose to split the pitch change between the mirrors, reflected in the design table as in increase in grating and secondary pitch angle magnitude to 0.993 degrees from 0.973 degrees. The practical result is that there is a 0.02 degree offset in pitch between the secondary reference surface and the $x$ axis that has to be accounted for in subsequent alignment (e.g., at the range).

## 1.2 Mirror Mounts

*MOSES* mirror mounts are mounted to a carbon fiber I-beam by way of threaded inserts embedded in the carbon fiber. The I-beam/insert structure is the Lockheed Optical Table System (LOTS). The threaded inserts are precisely located on a 4 inch grid with the mounting surfaces machined to be coplanar. Precision counterbores in the inserts accept shoulder screws for repeatable mount positioning. The I-beam and inserts thus form a precision optical bench, one capable of rocket flight. The grid axes and the normal to the mounting surfaces define *MOSES* coordinate axes. $+\hat{z}$ is normal to the insert mounting surfaces and $+\hat{x}$ points towards the sun. Angular coordinates of tip, tilt and roll are rotations about the $y$, $z$, and $x$ axis, respectively.

*MOSES* alignment strategy relies on LOTS grid and precision machined mounts to position the spectrograph components within mechanical tolerance. Fine alignment and focus is completed with kinematic adjustments build into the mirror mounts. The mirrors are mounted such that each is constrained in six places, to exactly constrain the six positioning degrees of freedom: the three spatial coordinates plus tip, tilt, and roll.

The constraint is made by a hemispherical ball bearing magnetically connected to the end of a bolt which is threaded into the mirror mount. A hollow cone is machined into the bolt end to allow the spherical surface to seat; the flat surface of the hemisphere is in contact with the mirror. Magnetic connection allows the hemisphere to readily pivot on the bolt end in order to seat flush with the mirror. The mirror is pressed against each constraint with an opposing vlier screw threaded into the mount on the opposite side of the mirror.

The position of the mirror in the mount can be adjusted by changing the depth to which the the constraint bolt is threaded into the mount. The depth of these bolts are set by precision shims which sit between mount and bolt head. Three constraints contact the face of each mirror in a tripod arrangement; these constrain the telescope angular alignment and focus. I had to make new shims for these constraint screws to optimize *MOSES-II* alignment and focus (chapter 3). The remaining three constraints – two on the bottom facet and one one on the side facet of each mirror – control mirror position transverse to the optic axis, as well as the roll. I was able to reuse the *MOSES-I* shims on these constraint screws.

## 1.3 Testing Tools

A brief description of my two principal optical testing tools.

### 1.3.1 Theodolite

A theodolite is an imaging telescope with reticle eyepiece mounted for rotation in altitude and azimuth. The angular coordinates are precisely measured; angular measurements approach 1" accuracy. The theodolite is often used in autocollimation mode, with an illuminated reticle projected from the telescope, retroreflected off of a flat mirror, and received again by the telescope, forming a reverse image of the reticle. When the two reticle images are aligned the theodolite is aligned to the mirror. I used a Leica Wild T-3000 theodolite for angular alignment measurements for *MOSES-II* optical testing.

### 1.3.2 Interferometer

I used a PhaseCam 6000 pixellated phase mask interferometer for nanometer precision measurements of optical surface figures in a poor vibration environment (second floor, clean room fans). The measurements are proportional to optical path differences between test and reference arms of the interferometer, caused by optical surface imperfections or alignment issues. Interferometry data is often analyzed by fitting the data to sets of orthogonal polynomials. In the following I use and make reference to the Zernike polynomials.

# CHAPTER 2

# *MOSES-II* OPTICAL TESTING

This chapter describes optical testing of the *MOSES* primary and secondary mirrors.

## 2.1 *MOSES-II* Primary Mirror

### 2.1.1 Radius of Curvature

The primary mirror radius of curvature determines the spectrograph focal length. The mirror mounts have limited focus adjustment, so it is important to accurately measure the radius of curvature. Nominal radius is 9.295 m. I used a tape measure, supported along its length, to measure the distance between primary mirror surface and center of curvature. The testing setup is shown in figure 2.1.

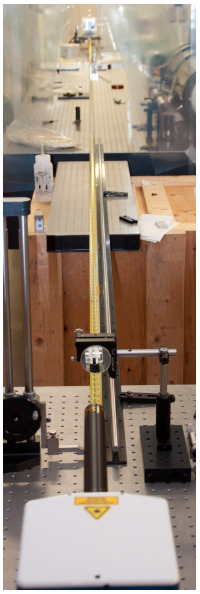

Figure 2.1: Test setup for measuring primary mirror radius of curvature.

I locate the center of curvature using an interferometer mounted with a diverging lens. The focal point of the diverging lens is coincident with the center of curvature of the primary when the Zernike defocus of the reflected wavefront is zero. I locate the diverger focal plane by translating a flat mirror along the optic axis near the focal plane until the Zernike defocus of the reflected wavefront is zeroed. The tape measure was run a few inches below the optical axis to avoid obscuration, and I use a height gage to vertically translate the "plane" of the primary mirror surface and diverger focal plane down to the tape, the difference in these measurements being the radius of curvature. The Zernike defocus between primary and interferometer suffered from noise probably due do vibration over the long measurement path. I improved the accuracy of the radius measurement by making several measurements in the neighborhood of correct radius, and fitting a line to the results. Measured radius is 9285 mm.

### 2.1.2 Figure

Primary mirror figure measurement was done with a PhaseCam 6000 phase shifting interferometer. In principle the measurements obtained in section 2.1.1 are measurements of the grating figure, but they are low resolution do to f/# mismatch between the interferometer diverging lens and primary mirror operated at its center of curvature (f/22 and f/120, respectively), so I used the testing arrangement shown schematically in figure 2.2.

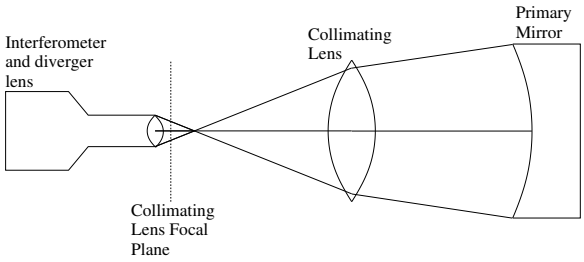


Figure 2.2: Test setup for measuring primary mirror surface figure.

The primary mirror figure measurements are corrupted by optical path length variation in the test setup. I contrived a reference measurement using the *MOSES-I* flight spare [Appendix?]. The mirror figure was out of specification, suffering from about 1.5 (46.5 nm) waves of astigmatism. The measured figure and Zernike fit is shown in the top row of 2.4.

### 2.1.3 Grating Figure Correction

The imaging characteristics of the primary mirror were expected to be poor, so we modified the primary mirror mount to accept vlier screws (spring loaded plungers, figure 2.3) and attempted to mechanically force the mirror to a better shape. With the primary mounted in the figure test configuration I experimented with different vlier screw positions and forces. I obtained significant reduction in the figure error using two screws. The measured primary mirror figure and Zernike fit following correction are shown in the bottom row of figure 2.4. The grating figure is analyzed in terms of expected instrument point spread functions in chapter 4.


Figure 2.3: Back plate of the primary mirror mount. The three threaded shafts are the vlier screws that push the primary against the tip/tilt/focus constraints. The grid of threaded holes accepts vlier screws to apply controlled forces to the back of the mirror in an effort to correct the distorted figure.

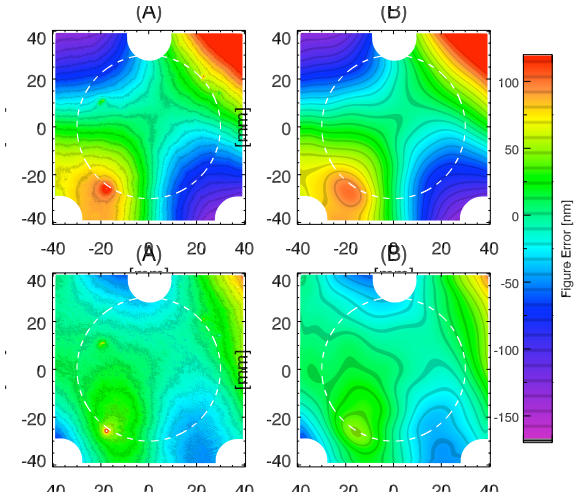


Figure 2.4: Left column: Pre (top) and post (bottom) correction measured primary figure error. Right column: 120 term Zernike polynomial fits, used to obtain a smooth representation of the data. The circular indents are obscuration by the tip/tilt/focus constraint screws. The central diffracting region of the mirror is visible in the measured figure as a 5 nm deep indent relative to the surrounding surface. The white dashed circle is a circular fit to points resulting from an edge finding exercise.

## 2.2 *MOSES-II* Secondary Mirror

### 2.2.1 Wedge Angle

I did the wedge angle measurement using a single theodolite and a precision corner cube. The testing setup is shown in figure 2.5. A theodolite in autocollimation mode is alternately aligned to the multilayer surface, then the reference surface by way of the corner cube. The wedge angle is the difference between these measurements. The secondary was mounted to permit translation into and out of the page, which I used to measure wedge angle variation at different locations along the mirror. Measured average wedge angle is 0.9738 degrees (0.973 degrees specified). 8 measurements at different locations along the y (dispersion) dimension of the mirror yields standard deviation about this value of 0.0002 degrees.

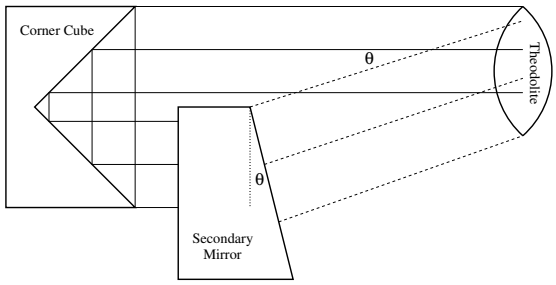


Figure 2.5: Test setup for measuring secondary wedge angle.

### 2.2.2 Figure

I measured the surface figure error of *MOSES-II* secondary mirror verified specification on aperture alignment, slope error and mid-scale roughness as per items 1, 2 and 3 of §4.3 of the MOSES-II Fold Flat Specification [MOSES-II FOLD FLAT SPEC]. The surface normals of the left and right sub-apertures are parallel with

that of the center sub-aperture to within a fraction of an arc second, well within the specified 5 arc seconds. Measured slope error is 1.38 $\mu$rad RMS, less than the specified 1.9 $\mu$rad RMS. Midscale roughness measures 0.71 nm RMS, less than the specification of 1.1 nm RMS.

Given the size of the secondary mirror I used a beam expander that allowed me to get the short dimension of the secondary within the interferometer field of view. The raw measurements of the secondary are dominated by systematic errors in the interferometer/beam expander system, and a reference image was required to see the true surface. I have a $\lambda/100$ flat mirror $F_R$ of sufficient reference quality, but it's diameter is smaller than the smallest dimension of the secondary.

I made a reference image by translating $F_R$ and making overlapping measurements of the reference surface across the interferometer field of view. I stitched the measurements together by optimizing the tip, tilt, and defocus of the reference measurements to minimize the mean absolute deviation in the overlap regions. Figure 2.6 shows the reference image measured thus, which is stitched together from 6 separate measurements.

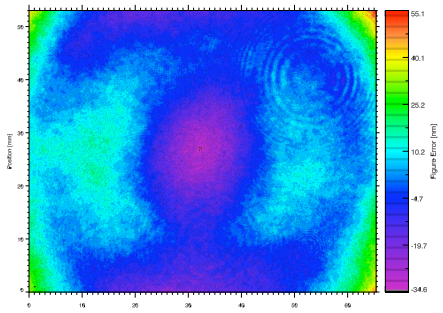


Figure 2.6: Measured interferometer reference, stitched together from 6 partial measurements of the beam. Area is 65.3 mm $\times$ 53.0 mm. WFE is 10.7 nm RMS and 89.7 nm PV.

I measured secondary in segments by translating the mirror across the interferometer beam. Each segment was reference subtracted and then stitched together like the reference image. The measured surface figure error of the secondary mirror is shown in figure 2.7

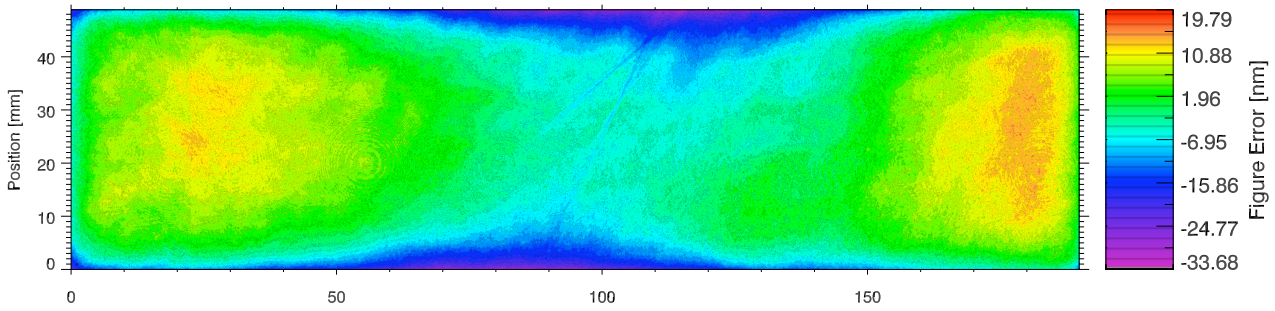


Figure 2.7: Measured *MOSES-II* figure error, composed of 7 measurements of overlapping segments of the mirror. Total area is 189.8 mm × 48.8 mm with image pixel resolution 73 $\mu$m. An imperfection in the stitching process can be seen around x = 22 mm. Tip and tilt have been subtracted.

Secondary mirror figure results are summarized in table 2.1.

*MOSES-II* Secondary Mirror Test Results

| Spec Description | Specification | Measured |
|---|---|---|
| Left Aperture Alignment | $<$ 5” | .03” |
| Right Aperture Alignment | $<$ 5” | .07” |
| Slope Error | $<$ 1.9 $\mu$rad RMS | 1.38 $\mu$rad |
| Midscale Roughness | $<$ 1.1 nm RMS | 0.71 nm |

Table 2.1: Summary of test results for *MOSES-II* secondary mirror.

# CHAPTER 3
# ALIGNMENT AND FOCUS

The critical mirror angular alignments, focus, and grating roll are described in this chapter. The optical prescription for *MOSES-II* is given in table 1.1. Alignment and focus were done without working CCDs due to failure of the *MOSES* command and data handling system, which was not repaired until after alignment was complete. The focus method described here is expected to be significantly more accurate than the method used prior. Improvement of spectrograph focus was noted as a major goal for the second flight in the *MOSES-I* final report [KANKELBORG MOSES I FINAL REPORT].

Spectrograph alignment in the dispersed orders depends on wavelength. The available alignment tools use visible wavelengths, so it's not possible to directly align the instrument in these orders. For the first flight, the system was aligned in the $m = 0$ order, and the outboard CCDs were then positioned relative to the $m = 0$ CCD according to the optical design, and the flight data show good relative focus [RUST PSF]. Reducing the primary mirror focal length does not significantly change the relative focal lengths (chapter 4), so I leave the CCDs fixed and optimize focus in $m = 0$ by changing the mirror separation.

Conceptually, alignment and focus is achieved in three steps:

1. Measure the alignment and focus state of the system from a known baseline (*MOSES-II* mirrors mounted with *MOSES-I* shims).

2. Measure the change in alignment with change in shim length.

3. Calculate new shim lengths, fabricate and install new shims, verify alignment and focus.

Alignment measurements are described in section §3.1. Focus measurement is described in §3.2.

## 3.1 Alignment

The coordinates in table 1.1 are referenced to LOTS axes. Two main alignment steps are required:

1. Align secondary mirror to LOTS
2. Align primary so rays parallel to $\hat{x}$ pass through the center of the $m = 0$ CCD.

### 3.1.1 Secondary to LOTS

*MOSES* spectrograph alignment is referenced to the secondary mirror alignment surface. The mount design is referenced to LOTS inserts. Therefore the secondary alignment surface has to be aligned to LOTS.

LOTS axes are measured with the tool shown in figure 3.1. Gage plugs in the insert counterbores and coplanar insert mounting surfaces keep s setup block square to LOTS axes. Gage blocks affixed to the setup block provide theodolite alignment surfaces. A theodolite aligned to the foremost gage block in figure 3.1 is looking parallel to $-\hat{x}$. Aligning a temporary reference mirror (e.g. upper left) then frees up the theodolite.

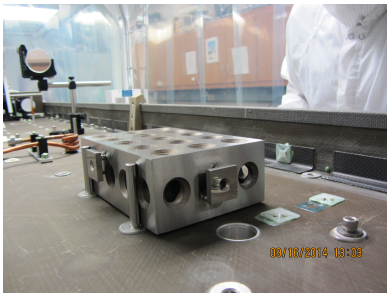

Figure 3.1: Alignment tool used to reference LOTS axes.

Once $\mathbf{x}$ is established I install the secondary mirror and measure the angular misalignment. Secondary mirror alignment is controlled by the tripod of constraint screws on the EUV surface. I had to calibrate the change in alignment to the change in shim length. I did this by using gage blocks as shims on each constraint screw in turn, measuring alignment change as I varied the gage block thickness in 0.001" increments. Now I can calculate the *relative* change in shim length required to align the secondary, but I can't calculate the absolute shim length until after I measure system focus. To proceed with alignment I temporarily align the secondary by slightly loosening one or more of the constraint screws.

### 3.1.2 Primary to Filter Tube Target

With the secondary aligned, the primary mirror must be aligned so that rays parallel to $\hat{x}$ are focused to the center of the $m = 0$ CCD. With the cameras inoperable I used a proxy for this alignment: a target engraved in an aluminum disc mounted to the end of the $m = 0$ order filter tube, shown in figure 3.2.

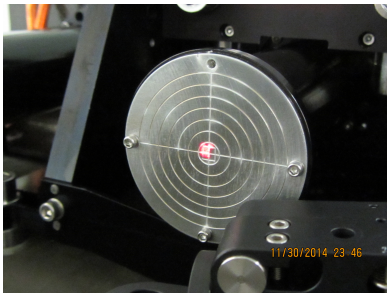


Figure 3.2: Filter tube alignment target. The central square is 3.63 mm on a side which corresponds to the width of the converging (square) beam at $x$=211.01 mm (the target $x$ location). The crosshairs are parallel to y and z. The circles have radii of integer multiples of 3 mm, corresponding to about 2.3' of misalignment, or a little under 10% of the field of view in the long $y$ direction.

I set up the theodolite so it is aligned along $-\hat{x}$ looking into the primary mirror and adjust the theodolite focus until the filter tube target is sharp. Angular misalignment of the primary is the angular difference relative to the target center, measured with the theodolite. As with the secondary mirror, the primary mirror pointing is controlled by the tripod of constraint screws on the EUV surface, and again I had to calibrate the change in shim length to the change in angular alignment. I did this in a similar fashion to the secondary angular alignment calibration, this time using 0.001" shim washers, as the 0.5" constraint screws do not accept gage blocks. This completes the required angular alignment measurements.

## 3.2 Focus

The shims which control angular alignment also determine the **x** location of the mirrors and thus spectrograph focus. Therefore system focus state must be known before the shim lengths can be adjusted properly.

Proper focus results in the smallest size spot on the CCD. Traditional focus methods rely on through focus spot size measurements where the optical path is changed and the resulting spot size is measured. The cameras were not operable so I came up with a different focus method shown in figure 3.3.

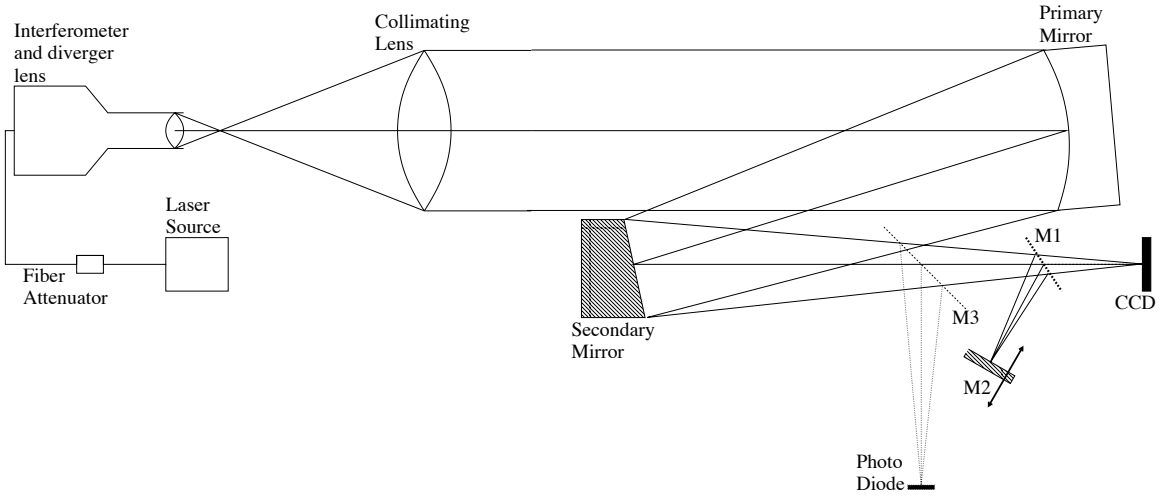


Figure 3.3: Test setup for focus. The initial wavefront defocus is precisely zeroed using a high quality flat mirror.

I use an interferometer to measure the curvature in an initially flat wavefront passed though the spectrograph and retro reflected by the CCD back to the interferometer. The Zernike defocus of the reflected wavefront is directly proportional to required change in shim length to achieve best focus. I calibrated the measurements by redirecting (with flat mirror M1) the converging beam to a flat mirror (M2) which is used to measure the wavefront Zernike defocus as M2 is precisely translated through the focus of the converging beam. This serves the same function as translating the CCD but is significantly easier and carries less risk for the sensitive camera system. The location of the measured spectrograph defocus on the calibration curve determines the required change in shim length to achieve focus. Figure 3.4 shows the

results of the focus measurement, using the *MOSES-I* shims as a baseline to focus the *MOSES-II* optics.

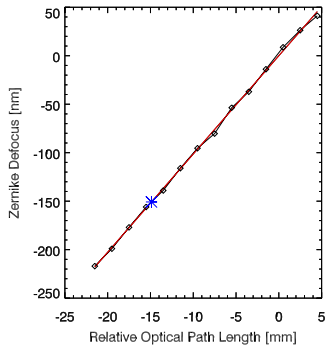


Figure 3.4: Points show measured Zernike defocus as mirror M2 is translated perpendicular to the optic axis (redirected by M1). Over-plotted red line is a linear fit.Asterisk at x=-15 shows the measured value of the Zernike defocus in the actual spectrograph. This result shows that the optical path length has to be increased by 15 mm. This focus curve is far more sensitive than, e.g., measuring visible light root mean square spot size for focus determination.

## 3.3 Image Quality Results

Alignment and focus were completed prior to repairs to *MOSES* flight computer, hence the cameras were inoperable. The first true images taken with the *MOSES-II* spectrograph were taken using the big collimator at White Sands Missile Range during our launch campaign. A sample image of a resolution test target is shown in figure 3.5. Pre and post flight visible light point spread functions were also measured at MSU, these are shown in the following chapter.

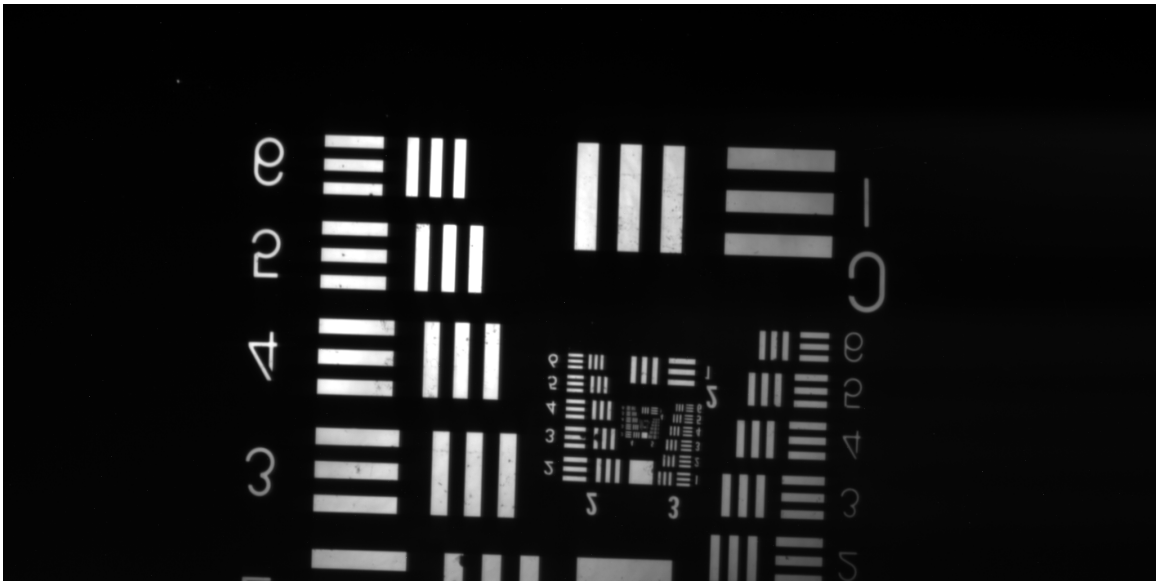

Figure 3.5: Air force resolution target of the aligned and focused *MOSES-II* spectrograph. Visible light, $m = 0$ spectral order.

## 3.4 Grating Roll Measurement

I verified that the grating roll angle put the dispersion in the $x - y$ plane by direct measurement. With a laser beam aligned to the optic axis, I used the LOTS alignment tool to align a stage (figure 3.6) to translate a CMOS camera parallel to the $y$ axis and precisely measured the height (z) of the diffracted beam in the $m = -1$ and $m = +1$ orders. The results (figure 3.7) show the dispersion plane is effectively parallel to the $x - y$ plane, as intended.

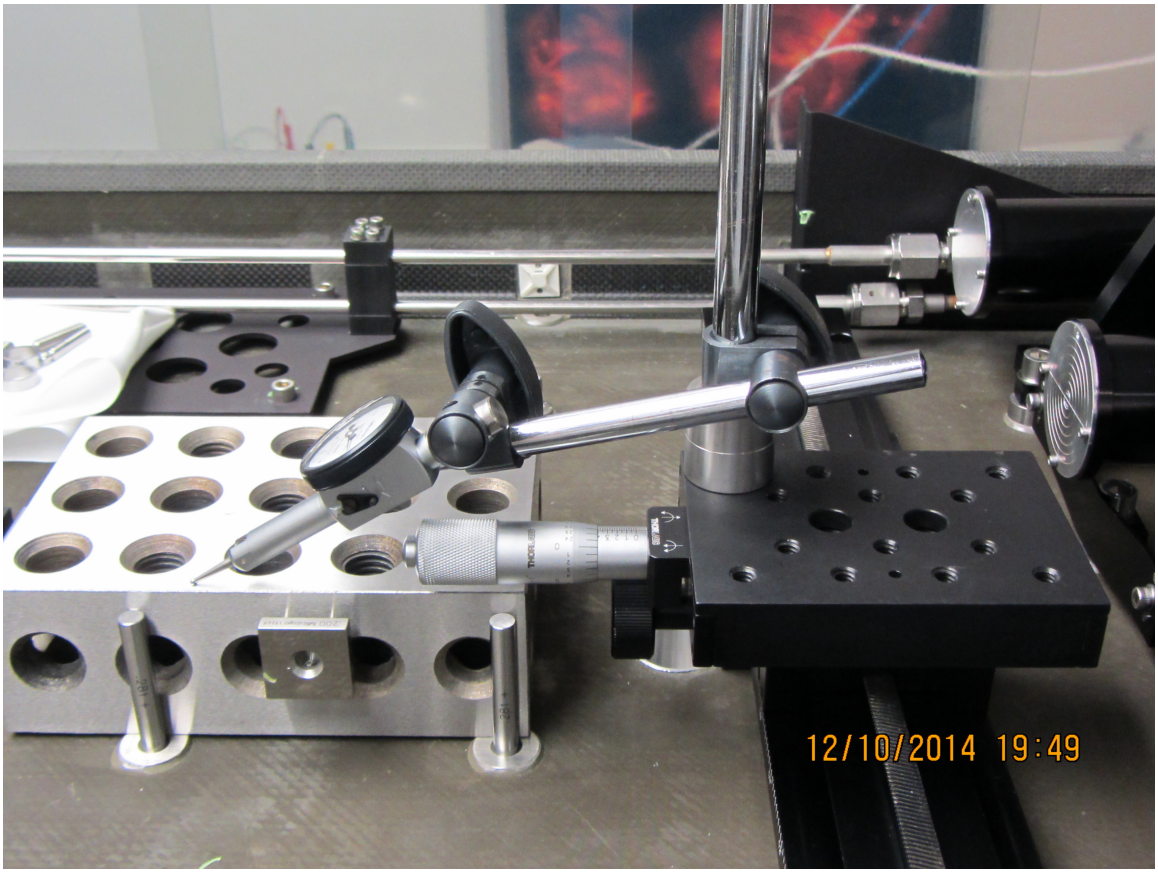


Figure 3.6: Alignment of translation stage for grating roll measurement.

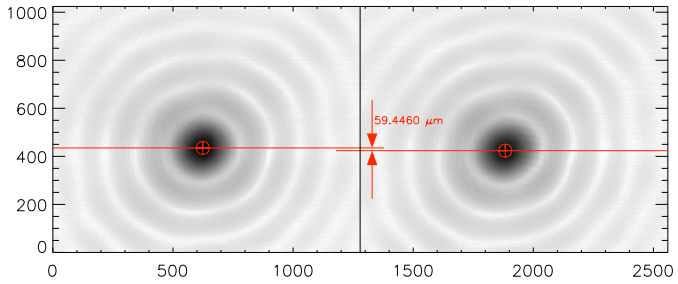


Figure 3.7: The figure shows images of a laser beam after diffraction from the grating in the $m = -1$ and $m = +1$ spectral orders. The camera was mounted to translate parallel to the y axis. The vertical difference in the spot image centroid in the two orders is practically zero, indicating good roll alignment of the primary mirror.

# CHAPTER 4
# OPTICAL MODELING

In this chapter I use a use a Fourier optics model to estimate optical performance of the *MOSES* spectrograph.

## 4.1 Fourier Optics Model

The electric field distribution near *MOSES* ideal focal plane due to a distant source of illumination is modeled as

$$E(\vec{f}+\vec{\delta}) = \iint E_0(y',z') e^{ik\left(|\vec{f}-\vec{r}|-\frac{m\lambda y'}{d}\right)} e^{-i2\pi\left(\frac{\delta_y}{\lambda f}y'+\frac{\delta_z}{\lambda f}z'\right)} dy'dz' \tag{4.1}$$

Here, $\vec{f}=(y,z,x)$ is the nominal focal point, $\vec{\delta}=(\delta_y,\delta_z,\delta_x)$ is a small displacement perpendicular to $\vec{f}$, $\vec{r}=(y',z',x'(y',z'))$ is the position vector on the surface of the grating, $m$ is the diffraction order, and $d$ is the grating pitch. The grating rulings are modeled a phase contribution which is linear along the dispersion direction. $E_0(y',z')$ is the incident electric field evaluated on the mirror surface, which for a unit amplitude plane wave is given by

$$E_0 = e^{i\vec{k}\cdot\vec{r}} \tag{4.2}$$

where $\vec{k}$ is the incident wave vector.

The integral on the right of 4.1 is a function of spatial frequencies $(v,w)=\left(\frac{\delta_y}{\lambda f},\frac{\delta_z}{\lambda f}\right)$ whose sampling interval and range are given by the usual sampling considerations, i.e.,

$$\delta v = \frac{1}{\Delta y'} \quad , \quad \Delta v = \frac{1}{\delta y'} \tag{4.3}$$

Given $\delta y', \Delta y', \delta z', \Delta z'$ as the sampling interval and range in the aperture plane the sampling interval and range in the focal plane are therefore given by

$$\delta\delta_y = \frac{\lambda f}{\Delta y'} \quad , \quad \Delta\delta_y = \frac{\lambda f}{\delta y'} \tag{4.4}$$

$$\delta\delta_z = \frac{\lambda f}{\Delta z'} \quad , \quad \Delta\delta_z = \frac{\lambda f}{\delta z'} \tag{4.5}$$

$\delta_x$ is given by the condition that $\vec{\delta} \cdot \vec{f} = 0$.

The diffraction code consists of the following steps:

- Define grating parameters, and grating and secondary positions and orientations.
- Define incident light wavevector based on input incidence angles (altitude and azimuth).
- Define grid of grating coordinates based on input desired number of points and maximum range of aperture coordinates.
- Estimate nominal focus position $\vec{f}$.
- Use optimization procedure to minimize the phase term under the integral in the diffraction formula as a function of $\vec{f}$, using the guess from the previous step as a starting point.
- Repeat steps 2-5 for several incident light directions spanning a 20' (azimuth) by 10' (altitude) field of view, and for each of the three spectral orders m = -1,0,1.
- Fold the calculated $\vec{f}$ vectors via the secondary mirror.

- Subtract off the vector $\vec{f_0}$, the (folded) position vector of the best focus for on axis illumination in the zero order. This step shifts the coordinate system origin to the center of the m=0 order detector.

- For each of the three spectral orders, fit a plane to the best focus positions. These planes give the detector positions and orientations.

## 4.2 Results - Optical Prescriptions

I tested the code by first modeling the *MOSES-I* spectrograph and comparing the results (Table 4.1 ) with the original ZEMAX model [ROGER THOMAS ZEMAX]. The Fourier model results are almost identical.

MOSES 1 Design Table from Fourier Optics Model

| Item | X | Y | Z | Pitch | Yaw |
|---|---|---|---|---|---|
| Grating | 118.8 | 0.0 | 78.5 | -0.973 | 0.0 |
| Secondary | 2428.7 | 0.0 | 0.0 | +0.973 | 0.0 |
| Det(+1) | 3.0 | -136.9 | 0.0 | -.003 | -2.480 |
| Det( 0) | 0.0 | 0.0 | 0.0 | -.001 | 0.000 |
| Det(-1) | 3.0 | +136.9 | 0.0 | -.003 | +2.478 |

Table 4.1: *MOSES-I* design table from Fourier optics model, using grating and secondary position and orientation from [ROGER THOMAS ZEMAX]. Grating radius of curvature is 9.48 m and grating pitch is 950 l/mm. Angles given are in degrees, and positions in mm.

I modeled *MOSES-II* with the secondary moved towards the detectors to accommodate the reduced focal length of the grating, and the grating and secondary tips

optimized to center the detectors at z=0. Table 4.2 shows the resulting optical design table. The outboard detectors are required to move in (towards $m = 0$) by about 2.7 mm or a loss of 10% of the usable field of view will result. The tip of the secondary should not present any extra difficulty in the optical alignment.

*MOSES-II* Design Table

| Item | X | Y | Z | Pitch | Yaw |
|---|---|---|---|---|---|
| Grating | 118.8 | 0.0 | 78.5 | -0.993 | 0.0 |
| Secondary | 2382.5 | 0.0 | 0.0 | +0.993 | 0.0 |
| Det(+1) | 2.9 | -134.2 | 0.0 | .005 | -2.478 |
| Det( 0) | 0.0 | 0.0 | 0.0 | -.001 | 0.000 |
| Det(-1) | 2.9 | +134.2 | 0.0 | .000 | +2.477 |

Table 4.2: MOSES 2 design table from Fourier optics model after moving secondary towards detectors to compensate for change in grating focal length, and adjusting the tip of the grating and secondary equally to center the detectors at z=0 . Grating radius of curvature is 9.295 m and grating pitch is 621 l/mm. Angles given are in degrees, and positions in mm.

## 4.3 Point Spread Functions

### 4.3.1 EUV, Modeled

I used the model to estimate point spread functions at operating wavelength across the field of view in each spectral order. I've shown the model results from *MOSES-I* (figure 4.1) and *MOSES-II* (figure 4.2) to show how the change the grating changes the expected instrument point spread functions. Limiting the aperture in the dispersed

orders tightens up the point spread functions; conversely, the central order point spread function is expected to get a little worse as the aperture in that order is limited.

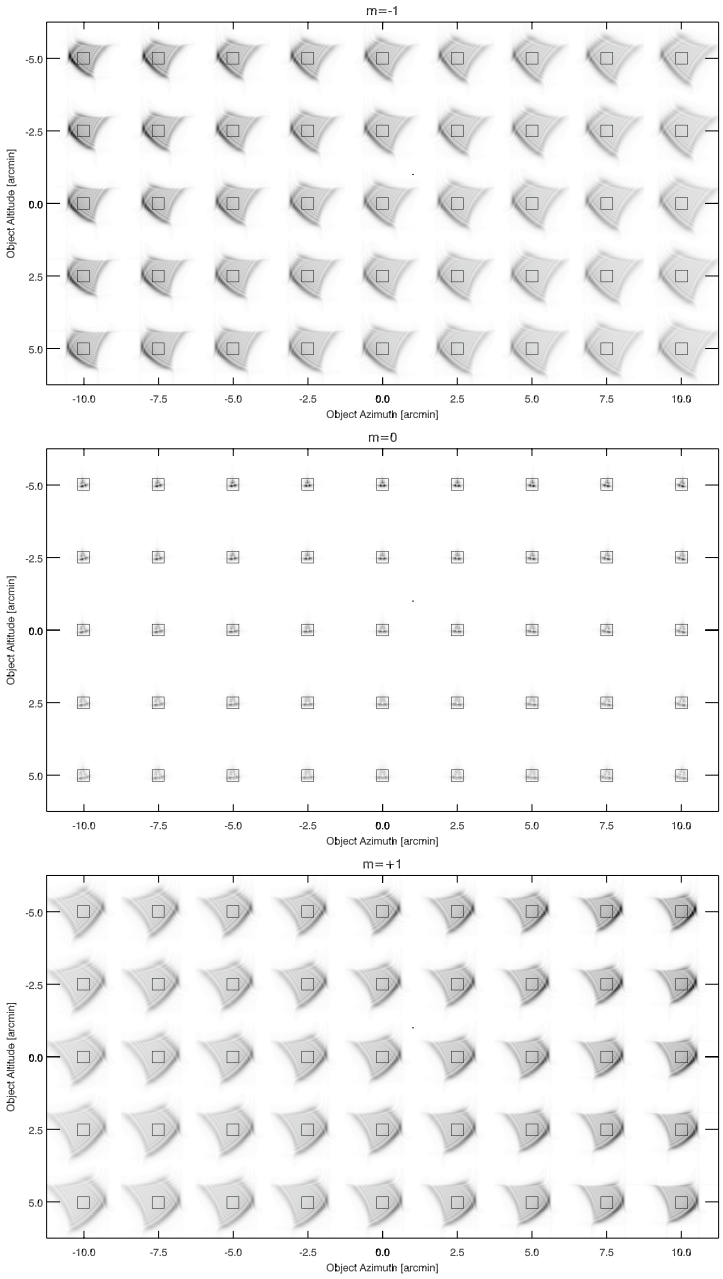


Figure 4.1: Point spread functions in *MOSES-I* three orders for varying field angle. Viewpoint is facing detectors, sun at your back, with positive z towards the top of the page. Superimposed squares represent 13.5 micron MOSES pixels.

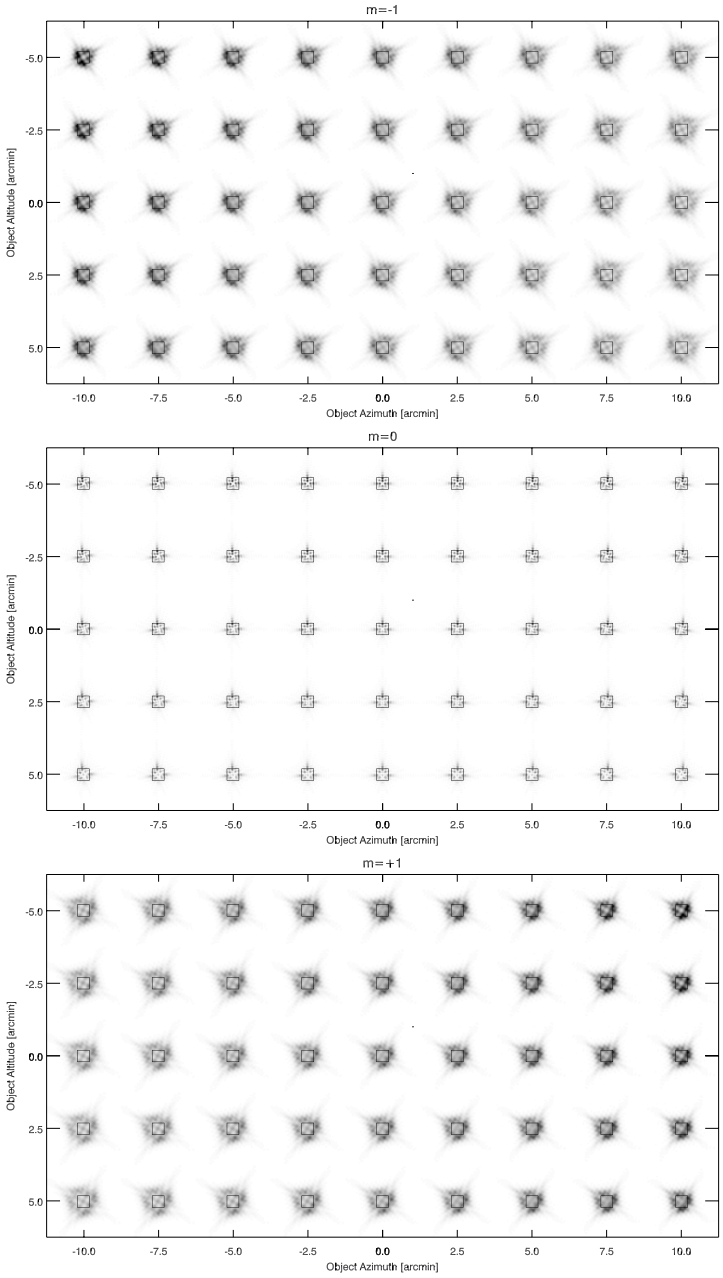


Figure 4.2: Point spread functions in *MOSES-II* three orders for varying field angle using the optical design from table 4.2. Viewpoint is facing detectors, sun at your back, with positive z towards the top of the page. Superimposed squares represent 13.5 micron MOSES pixels.

I incorporated the measured figure error of the primary mirror (shown in figure 2.4) into the model as added path difference, and estimated point spread functions pre and post correction. These results are shown in figure 4.3 with spatial sampling of 13.5 $\mu m$ (*MOSES* CCD sampling).

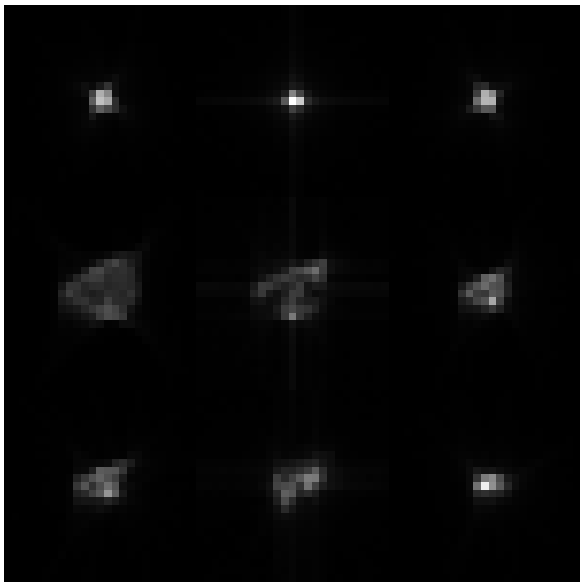

Figure 4.3: Modeled EUV point spread functions. Top Row: point spread functions from perfect primary mirror. Center Row: point spread functions using measured primary mirror figure (§2.1.2). Bottom Row: point spread functions using corrected primary mirror figure (§2.1.3). Left to right column: $m = -1$, $m = 0$, $m = +1$. All point spread functions are normalized to total of one and displayed on the same scale.

The correction shows great promise for improving *MOSES-II* image quality.

### 4.3.2 Visible Light, Measured and Modeled

Subsequent to alignment, and prior to going to the range, undergraduate student Roy Smart and I measured the $m = 0$ point spread function in visible ($\lambda = 635nm$)

light. An interferometer and beam expander arrangement was used, so precise collimation was achieved by adjusting the system until the measured Zernike defocus of a high quality flat mirror interposed into the beam was zero. We repeated the measurement post flight, and also thought to obscure the central diffracting region of the primary mirror, so the $m = 0$ aperture was approximately as it is at operational wavelength. The results are shown in figure 4.4.

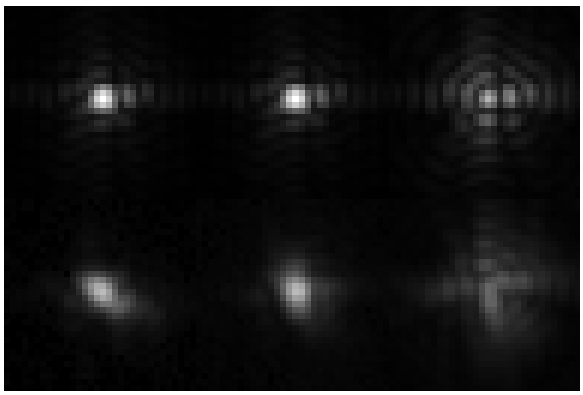

Figure 4.4: Top Row from model: Full aperture, full aperture, central obscuration. Bottom Row measured: Full aperture pre flight, full aperture post flight, central obscuration post flight. Left to right column: $m = -1$, $m = 0$, $m = +1$. All point spread functions are normalized to total of one and displayed on the same scale.

## 4.4 Distortion Modeling

Optical distortion could be an issue with the MOSES spectrograph which is sensitive to alignment between spectral orders. I modeled the optical distortion in *MOSES-I* by comparing focus spot centroids in the detector planes as a function of field angle – $m = -1$ relative to $m = 0$ (figure 4.5), and $m = +1$ relative to $m = 0$ (figure 4.5). The model shows a ramp in distortion which reaches a magnitude of approximately

1 pixel towards the corners of the field of view. The *MOSES* digital co-alignment routine employs a linear warping of the images to minimize the impact of distortion. This type of model could be useful to constrain the co-alignment.

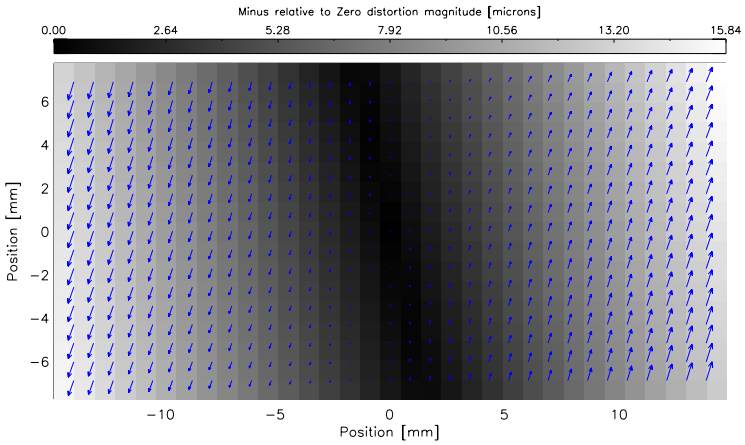


Figure 4.5: Optical distortion in *MOSES-I*

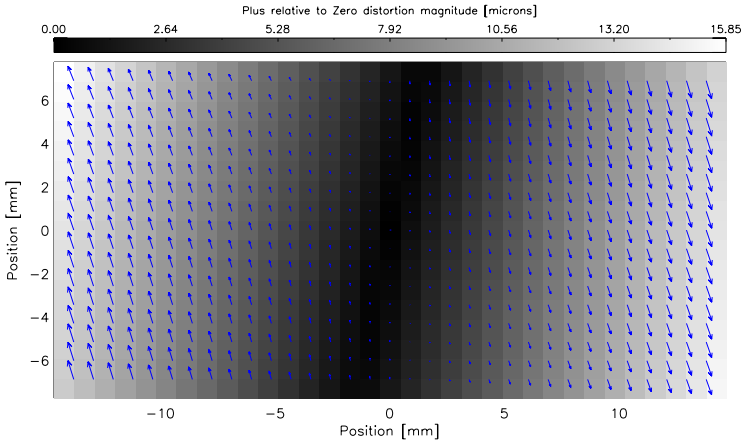


Figure 4.6: example